

Lattice Boltzmann modeling of two-phase electrohydrodynamic flows under unipolar charge injection

Kang Luo, Yu Zhang, Jian Wu , Hong-Liang Yi ,* and He-Ping Tan

*School of Energy Science and Engineering, Harbin Institute of Technology, Harbin 150 001, People's Republic of China
and Key Laboratory of Aerospace Thermophysics, Harbin Institute of Technology, Harbin 150 001,
People's Republic of China*

 (Received 26 February 2022; accepted 1 June 2022; published 23 June 2022)

In this work, a two-dimensional droplet confined between two parallel electrodes under the combined effects of a nonuniform electric field and unipolar charge injection is numerically investigated using the lattice Boltzmann method (LBM). Under the non-Ohmic regime, the interfacial tension and electric forces at the droplet surface cooperate with the volumetric Coulomb force, leading to complex deformation and motion of the droplet while at the same time inducing a bulk electroconvective flow. After we validate the model by comparing with analytical solutions at the hydrostatic state, we perform a quantitative analysis on the droplet deformation factor D and bulk flow stability criteria T_c under different parameters, including the electric capillary number Ca , the electric Rayleigh number T , the permittivity ratio ε_r , and the mobility ratio K_r . It is found that the bulk flow significantly modifies the magnitude of D , which in turn decreases T_c of the electroconvective flow. For a droplet repelled by the anode, $\varepsilon_r > 1$, an interesting linear relationship can be observed in the D - Ca curves. However, for a droplet attracted to the anode, $\varepsilon_r < 1$, the system is potentially unstable. After first evolving into a quasisteady state, the droplet successively experiences steady flow, periodic flow, second steady flow, and oscillatory flow with increasing T . Moreover, discontinuities can be observed in the D - T curves due to the transitions of bulk flow.

DOI: [10.1103/PhysRevE.105.065304](https://doi.org/10.1103/PhysRevE.105.065304)

I. INTRODUCTION

Electric fields, when applied to weakly conducting dielectric liquids, can give rise to fluid motions, the study of which forms the field of electrohydrodynamics (EHD) [1,2]. Under the assumption of Ohmic conduction, Taylor and Melcher [1] developed the well-known leaky dielectric model (LDM) to explain the behavior of droplets under a steady electric field. The original LDM includes the Stokes equations for fluid motion and an expression for current conservation. Charges are carried to the interface by conduction. The tangential electric field acts upon these charges to generate the shear stress that drags the EHD flow both inside and outside the droplet. The LDM achieves success in multiphase EHD problems due to its simplicity and qualitative agreement with experimental observations [3–5]. Since then, numerous computational and theoretical studies have been conducted based on LDM to predict different EHD problems [5–17]. However, as mentioned in the review of LDM by Saville [2], although the qualitative aspects of the LDM theory were vindicated, the quantitative agreement was very disappointing. Several possible reasons for the discrepancies were suggested by Saville [2], such as nonlinear surface charge convection, boundary conditions, electrokinetic effects, and space charge in the bulk. The former three possible reasons have been well discussed in a series of subsequent works. But the possible effect of bulk free charges is seldom mentioned because the basic assumption

of LDM, i.e., the Ohmic conduction assumption, is no longer valid.

The study of EHD problems beyond the Ohmic conduction regime has attracted much less attention. As reported in experimental measurements of the conductivity of dielectric liquids [18], the current-voltage I - V characteristics can be simply separated into the Ohmic region and the non-Ohmic region (see Fig. 1). In the Ohmic region, electric current is linearly proportional to the applied voltage. Then, there will be a saturation voltage V_s at which the linear relationship ends due to the limitations of the ion creation rate in the liquid volume. The value of V_s can be approximately determined by the competition between the charge relaxation time $\tau_c (= \varepsilon/\sigma)$ and the charge drift time $\tau_k (= l^2/KV)$, where l , ε , σ , and K are the distance between two electrodes, the permittivity, the conductivity, and the mobility, respectively. At $\tau_k \leq \tau_c$, the ions can span the gap between two electrodes before recombination, with the equals sign corresponding to the saturation voltage $V_s = \sigma l^2/K\varepsilon$. For $V > V_s$, the I - V curve goes to the non-Ohmic conduction regime, and free charges can exist both in the bulk and the interface. Other mechanisms such as charge injection or field-enhanced dissociation need to be considered. They lead to an increase in the current that is a nonlinear function of the applied voltage, which results in a steeper slope in I - V curves as reproduced in Fig. 1.

Charge injection, which originates due to the electrochemical reaction at the liquid/electrode interface, is an important mechanism of charge transport above V_s . In single-phase dielectric liquid, charge injection induced electroconvection (EC) has been well studied. Two-dimensional (2D) electro-

*Corresponding author: yihongliang@hit.edu.cn

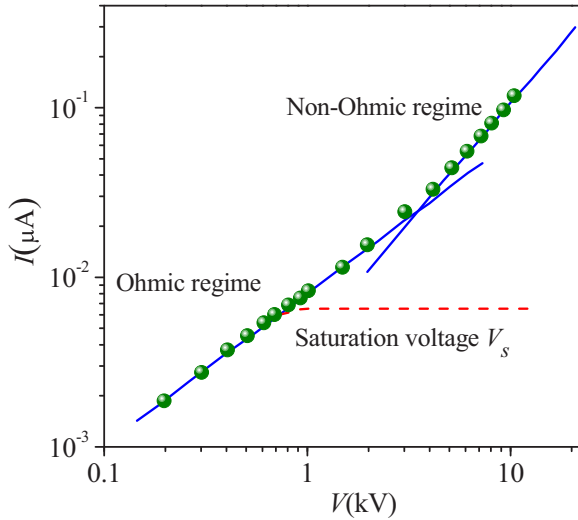


FIG. 1. The I - V characteristics in the experimental results of McCluskey *et al.* [18]. The horizontal dashed line corresponds to the saturation voltage. The steeper slope above the saturation voltage is characteristic of an injection process.

convective rolls [19–24] or three-dimensional (3D) cellular patterns [25–27] can be observed when the governing parameter T (the electric Rayleigh number) exceeds its linear stability threshold T_c . Extensive studies have been devoted to this problem from the standpoints of stability analysis, experimental study, and numerical study. Among those studies, linear and nonlinear stability analysis techniques have been conducted since the 1970s [23,28,29]. Results indicate that the electroconvective instability depends on various factors, such as the injection strength, the physical property parameters (e.g., ionic mobility and dielectric permittivity), and the residual conductivity. Previous experimental studies were focused mainly on the measurement of electroconvective heat transfer enhancement [18,30]. It is shown that the heat transfer rate was significantly increased (up to an order of magnitude) for all test cases considered in those studies [18]. In terms of numerical simulation, most results are obtained with methods based on a direct discretization of the partial differential equations, such as the finite-difference method [31], the finite-element method [32], and the finite-volume method (FVM) [20,21,33]. Recently, some particle-based methods were introduced into this field, such as dissipative particle dynamics (DPD) [34] and the lattice Boltzmann method (LBM) [24,35,36].

In the present study, we are interested in multiphase EHD phenomena in the non-Ohmic regime. Unipolar charge injection serves as the source of free space charges. When compared to the commonly used LDM, the space charges lead to some complex physical processes, such as the bulk electrical forces, bulk electroconvective flow, and related instabilities under high electric field. The governing equations, including Navier-Stokes equations for fluid flow, the Nernst-Planck equation for charge conservation, and the Poisson equation, are fully coupled both in the interface and in bulk liquid. Instead of Ohmic conduction, charges transfer within the liquid through three distinct mechanisms, i.e., convection,

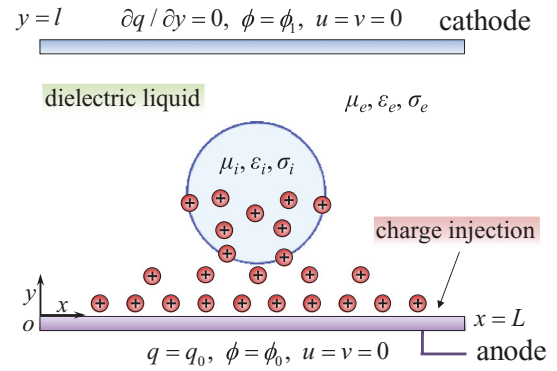


FIG. 2. Schematic diagram of the problem: a two-dimensional droplet confined between a charge-injecting anode and a charge-blocking cathode.

migration, and diffusion. Simulations are conducted in the framework of the unified LBM that we developed in [37–39].

The motivation of this work is threefold: (i) to consider the effects of charge-injection-induced bulk convective flow on droplet/bubble dynamics, (ii) to extend the study of electroconvective instability from the single-phase to the multiphase EHD system, and (iii) to develop a numerical model in the framework of LBM to simulate the coupling between droplet motion and deformation under an electric field. The rest of the paper is organized as follows. In Sec. II, the physical model, mathematical equations, and numerical methods are presented in detail. In Sec. III, results and discussions about the hydrostatic solutions, transient droplet motion, steady-state droplet deformation, as well as bulk electroconvective flow under different conditions are provided in detail. In Sec. IV, we provide our conclusions.

II. PHYSICAL MODEL AND MATHEMATICAL EQUATIONS

The problem considers a dielectric liquid layer of thickness l enclosed between two planar metal electrodes. A potential difference $V = \Delta\phi = \phi_0 - \phi_1$ is applied between the two electrodes. Figure 1 shows typical current-voltage characteristics where a linear part is the Ohmic regime [18]. After the saturation voltage V_s , I increases faster than Ohmically, due to the ion injection mechanism as reported by Felici [40].

As shown in Fig. 2, a liquid droplet is initially suspended in the center of the dielectric liquid layer. The dynamic viscosity, dielectric permittivity, and mobility of the carrying liquid are denoted by μ , ε , and K , respectively, and subscripts “ i ” and “ e ” are used to distinguish the inner and external parts of the droplet. The electrochemical reaction at the electrode-liquid interface (one side or both sides) leads to the generation of free charges that will be injected into the bulk of the liquid. Free charges may exist both in the bulk liquid and the surface depending on the property of the drop and the carrying liquid. The injected charges transfer within the liquid through three distinct mechanisms, i.e., convection, migration, and diffusion.

A. Governing equations and nondimensionalization

The dynamic behavior of a drop in dielectric liquids is governed by the fully coupled electrical and mechanical equations. The electrical equations include the Poisson equation for electric potential and the charge conservation equation [2], written as follows:

$$\nabla \cdot \varepsilon \mathbf{E} = q, \quad (1)$$

$$\begin{aligned} \nabla \times \mathbf{E} &= 0, \\ \frac{\partial n^{(k)}}{\partial t} + \mathbf{u} \cdot \nabla n^{(k)} &= \nabla \cdot [-\omega^{(k)} e z^{(k)} n^{(k)} \mathbf{E} + \omega^{(k)} k_B T \nabla n^{(k)}] \\ &+ r^{(k)}, \quad k = 1, \dots, N, \end{aligned} \quad (2)$$

where $n^{(k)}$, $\omega^{(k)}$, and $z^{(k)}$ are the concentration, mobility, and valence of k th species, and k_B , e , and T are the Boltzmann constant, electron charge, and fluid temperature, respectively. N is the total number of charge species. Three terms on the right side of Eq. (2) represent ion migration under an electric field, migration due to thermal diffusion, and production due to chemical reactions, respectively.

As concluded in Saville's review [2], two simplified forms of Eq. (2) are commonly used in different EHD problems, namely the *binary z-z electrolyte* in the leaky dielectric model [2] and the *single ionic specie* in the unipolar injection model. Although only the injection case in Eq. (3) is studied in this work, equations for the leaky dielectric model are also provided in Eq. (5) for comparison purposes.

For the *unipolar injection* case in the non-Ohmic regime, we have $N = 1$ and $r^{(k)} = 0$ by defining the total mobility $K = \omega e z$, the charge density $q = e z n$, and the charge diffusion $d = \omega k_B T$, and we have the Nernst-Planck equation as

$$\frac{\partial q}{\partial t} + \mathbf{u} \cdot \nabla q = \nabla \cdot (-K q \mathbf{E} + d \nabla q). \quad (3)$$

For *binary z-z electrolyte* in the Ohmic regime, three kinds of species $N = 3$ and $r^{(k)} = 0$ —namely the neutral, the cation, and the anion with concentrations of n_0 , n_+ , and n_- —are diluted in the fluid. Define the charge density q , conductivity σ , and charge diffusion coefficient d as follows:

$$q = \sum_k e z^{(k)} n^{(k)}, \quad \sigma = e^2 (\omega_+ n_+ + \omega_- n_-), \quad d = \omega k_B T. \quad (4)$$

Then, Eq. (2) in the Ohmic regime can be simplified to

$$\frac{\partial q}{\partial t} + \mathbf{u} \cdot \nabla q = \nabla \cdot (-\sigma \mathbf{E} + d \nabla q). \quad (5)$$

In most studies of steady drop deformation by LDM [41,42], the charge convection term and the charge diffusion term were neglected. Equation (5) can be further simplified to $\nabla \cdot (\sigma \mathbf{E}) = 0$.

Assuming both fluids are immiscible and incompressible, the continuity and momentum balance equations in the dimensional form are expressed as

$$\nabla \cdot \mathbf{u} = 0, \quad (6a)$$

$$\begin{aligned} \frac{\partial(\rho \mathbf{u})}{\partial t} + \nabla \cdot (\rho \mathbf{u} \mathbf{u}) &= -\nabla \hat{p} + \nabla \cdot (\mu \nabla \mathbf{u}) + \gamma \kappa \mathbf{n} \delta_s + q \mathbf{E} \\ &- \frac{1}{2} E^2 \nabla \varepsilon - \rho g \mathbf{e}_y. \end{aligned} \quad (6b)$$

The last four terms in Eq. (6b) indicate, from left to right, the surface tension force, the Coulomb force, the dielectric force, and gravity, respectively. To reduce the complexity of the problem, the effect of gravity is neglected in this work under strong unipolar charge injection. γ is the interfacial tension, κ is the local curvature of the interface, and δ_s is the Dirac delta function. \hat{p} denotes the generalized pressure, including the hydrostatic pressure and the extra electrostrictive contribution [43],

$$\hat{p} = p - \frac{1}{2} \rho E^2 \left(\frac{\partial \varepsilon}{\partial \rho} \right)_T. \quad (7)$$

The diffuse interface method [44], in which the interfacial region is spread onto a finite number of grid points, has been adopted in this paper. In this method, a wide variety of interfacial phenomena have been successfully applied [44]. In this manner, the variation of physical properties at the interface is smooth, and the whole domain can be treated as one region to avoid complex interface coupling. Using the density of fluid as an index function, the dielectric properties can be expressed as [11]

$$\begin{aligned} \varepsilon(\rho) &= \frac{\rho - \rho_i}{\rho_e - \rho_i} \varepsilon_e + \frac{\rho - \rho_e}{\rho_i - \rho_e} \varepsilon_i, \\ K(\rho) &= \frac{\rho - \rho_i}{\rho_e - \rho_i} K_e + \frac{\rho - \rho_e}{\rho_i - \rho_e} K_i. \end{aligned} \quad (8)$$

B. Analysis of timescales and nondimensionalization

Different physical processes involved in the EHD problem have different timescales, including the viscous time t_μ , the charge relaxation time t_r , the capillary time t_c , the electrostatic time t_e , the charge migration time t_k , and the charge diffusion time t_d , defined as

$$\begin{aligned} t_\mu &= l^2 \rho / \mu, \quad t_r = \varepsilon / \sigma, \quad t_c = l \mu / \gamma, \\ t_e &= \mu / \varepsilon E^2, \quad t_k = l^2 / K \Delta \phi, \quad t_D = l^2 / d. \end{aligned} \quad (9)$$

By choosing the characteristic time of the system to be the charge migration time $t_k = l^2 / K \Delta \phi$, the distance between two electrodes l is the characteristic length. Then, parameters are made dimensionless by making the following transformations:

$$\begin{aligned} x_i^* &= \frac{x_i}{l}, \quad t^* = \frac{t K \Delta \phi}{l^2}, \quad u_i^* = \frac{u_i l}{K \Delta \phi}, \quad E_i^* = \frac{E_i l}{\Delta \phi}, \\ p^* &= \frac{p l^2}{\rho K^2 \Delta \phi^2}, \quad q^* = \frac{q l^2}{\varepsilon \Delta \phi}, \quad \rho^* = \frac{\rho}{\rho_e}, \\ \varepsilon^* &= \frac{\varepsilon}{\varepsilon_e}, \quad K^* = \frac{K}{K_e}. \end{aligned} \quad (10)$$

It should be noted that the characteristic length and time in the present work are different from those in Taylor's leaky dielectric model [2], in which the drop radius a and the electrostatic time t_e are taken as the characteristic length and time, respectively. The nondimensional system with five

nondimensional governing parameters can be given as

$$T = \frac{\varepsilon(\phi_0 - \phi_1)}{\mu K}, \quad \text{Ca} = \frac{l\varepsilon_0 E_0^2}{\gamma}, \quad C = \frac{q_0 H}{\varepsilon E_0},$$

$$M = \frac{1}{K} \left(\frac{\varepsilon}{\rho} \right)^{1/2}, \quad \alpha = \frac{d}{K \Delta \phi}. \quad (11)$$

The electric Rayleigh number T is defined as the ratio between the Coulomb force and the viscous force; the electric capillary number Ca stands for ratio of the electric force to the surface tension force; C represents the injection strength; M is the nondimensional mobility parameter, which is the ratio of the so-called hydrodynamic mobility to the actual ionic mobility; and α is the nondimensional charge-diffusion number with its typical value in the range between 10^{-3} and 10^{-4} [45].

An additional four parameters related to the ratio between internal and external physical properties, namely the dynamic viscosity ratio, the fluid density ratio, the permittivity ratio, and the mobility ratio, are defined as

$$\lambda = \frac{\mu_i}{\mu_e}, \quad \rho_r = \frac{\rho_i}{\rho_e}, \quad \varepsilon_r = \frac{\varepsilon_i}{\varepsilon_e}, \quad K_r = \frac{K_i}{K_e}. \quad (12)$$

Then, the governing equation given in Eqs. (1), (3), and (6) can be written in dimensionless form as (for clarity, the star symbol is omitted)

$$\nabla^2 \phi = -q, \quad \mathbf{E} = -\nabla \phi, \quad (13a)$$

$$\frac{\partial q}{\partial t} + \mathbf{u} \cdot \nabla q = \nabla \cdot (-q\mathbf{E}) + \alpha \nabla^2 q, \quad (13b)$$

$$\nabla \cdot \mathbf{u} = 0, \quad (13c)$$

$$\frac{\partial(\rho\mathbf{u})}{\partial t} + \nabla \cdot (\rho\mathbf{u}\mathbf{u}) = -\nabla \hat{p} + \frac{M^2}{T} \nabla^2 \mathbf{u} + \frac{M^2}{Ca} \gamma \kappa \mathbf{n} \delta_s$$

$$+ M^2 \left(q\mathbf{E} - \frac{1}{2} E^2 \nabla \varepsilon \right). \quad (13d)$$

Equations in the interface satisfy

$$\|\varepsilon \mathbf{E}\| \cdot \mathbf{n} = q_s, \quad \|\mathbf{E}\| \times \mathbf{n} = 0, \quad (13e)$$

$$\frac{\partial q_s}{\partial t} + \mathbf{u} \cdot \nabla_s q_s - q_s \mathbf{n} \cdot (\mathbf{n} \cdot \nabla) \mathbf{u} = \|\mathbf{E}\| \cdot \mathbf{n} + \alpha \nabla q_s \cdot \mathbf{n}, \quad (13f)$$

where $\|(\cdot)\|$ denotes the jump, “outside-inside,” of (\cdot) across the boundary, and \mathbf{n} is the local outer normal. ∇_s and q_s are the surface gradient and surface charge density, respectively [2]. It should be noted that the interface equations (13e) and (13f) can be combined into Eq. (13d) in the diffuse interface method.

C. Lattice Boltzmann method for multiphase EHD

As an approach at the mesoscopic level, the LBM studies the microdynamics of fictitious particles by using simplified kinetic models [46,47]. The kinetic nature brings many distinctive features to the LBM, such as the clear picture of streaming and collision processes of simulated fluid particles, the simple algorithm structure, the easy implementation of boundary conditions, and the natural parallelism.

These appealing features make the LBM a powerful numerical tool for simulating multiphase and multifield coupling fluid systems [46,47]. Many multiphase LBMs based on the diffuse-interface scheme have been developed in the past two decades [47–49], including the pseudopotential LBM [50–53], the color-gradient LBM [41,54], the free-energy LBM [55], and the phase-field LBM [42,56–58]. In this work, the pseudopotential LBM is adopted due to its simplicity and ease of implementation. In addition, to reduce the spurious velocity at curved interfaces, the MRT collision operator and the changeable parameter a in the Carnahan-Starling equation of state are also used to control the thickness of the diffuse interface [59].

Equations for the pseudopotential LBM have been well established. Here we just provide some of the main formulas; for more detailed equations, please refer to Ref. [60]. The evolution equation of the density distribution function can be written as

$$f_i(\mathbf{x}_i + \mathbf{c}_i \Delta t, t + \Delta t) - f_i(\mathbf{x}_i, t)$$

$$= -\bar{\Lambda}_{ij} (f_j - f_j^{\text{eq}})|_{(x,t)} + \left(I_{ij} - \frac{1}{2} \bar{\Lambda}_{ij} \right) S_j \Big|_{(x,t)} \Delta t, \quad (14)$$

where f and f^{eq} are the density distribution function and its equilibrium distribution, respectively. \mathbf{I} is the unit tensor, and \mathbf{S} is the forcing term. $\bar{\Lambda} = \mathbf{M}^{-1} \Lambda \mathbf{M}$ is the collision matrix, where \mathbf{M} is an orthogonal transformation matrix and Λ is a diagonal matrix given as [59]

$$\Lambda = \text{diag}(\tau_g^{-1}, \tau_e^{-1}, \tau_\zeta^{-1}, \tau_j^{-1}, \tau_q^{-1}, \tau_j^{-1}, \tau_q^{-1}, \tau_v^{-1}, \tau_v^{-1}). \quad (15)$$

The commonly used D2Q9 model [61] is applied to the discretization of velocity space in two dimensions. The equilibrium distribution function [62] in Eq. (14) may be expressed as

$$f_j^{\text{eq}} = \rho \omega_j \left(1 + \frac{\mathbf{c}_j \cdot \mathbf{u}^{\text{eq}}}{c_s^2} + \frac{(\mathbf{c}_j \cdot \mathbf{u}^{\text{eq}})^2}{2c_s^4} - \frac{(u^{\text{eq}})^2}{2c_s^2} \right),$$

$$j = 1 - 9. \quad (16)$$

Macroscopic quantities, such as the fluid density, the calculated velocity, the velocity for equilibrium distribution, and the real fluid velocity, are expressed, respectively, as

$$\rho = \sum_j f_j \mathbf{u} = \frac{1}{\rho} \sum_j \mathbf{c}_j f_j \mathbf{u}^{\text{eq}} = \mathbf{u} + \frac{\tau \mathbf{F}}{\rho} \mathbf{u}^p = \mathbf{u} + \frac{1}{2\rho} \mathbf{F} \Delta t. \quad (17)$$

The forcing term in Eq. (14) can be given in the velocity space. Using the GZS scheme [63], we have

$$S_j = \omega_j \left(\frac{\mathbf{c}_j - \mathbf{u}^{\text{eq}}}{c_s^2} + \frac{\mathbf{c}_j \mathbf{u}^{\text{eq}}}{c_s^4} \right) \cdot \mathbf{F} \Delta t, \quad (18)$$

where $\mathbf{F} = \mathbf{F}_{\text{int}} + \mathbf{F}_{\text{ele}}$ is the total force acting on the system, including the interparticle force \mathbf{F}_{int} and the external electric force \mathbf{F}_{ele} [64], defined as

$$\mathbf{F}_{\text{ini}}(\mathbf{x}) = -g\psi(\mathbf{x}, t) c_s^2 \sum_j w_j \psi(\mathbf{x} + \mathbf{c}_j) \mathbf{c}_j,$$

$$\mathbf{F}_{\text{ele}}(\mathbf{x}) = q\mathbf{E} - \frac{1}{2} E^2 \nabla \varepsilon. \quad (19)$$

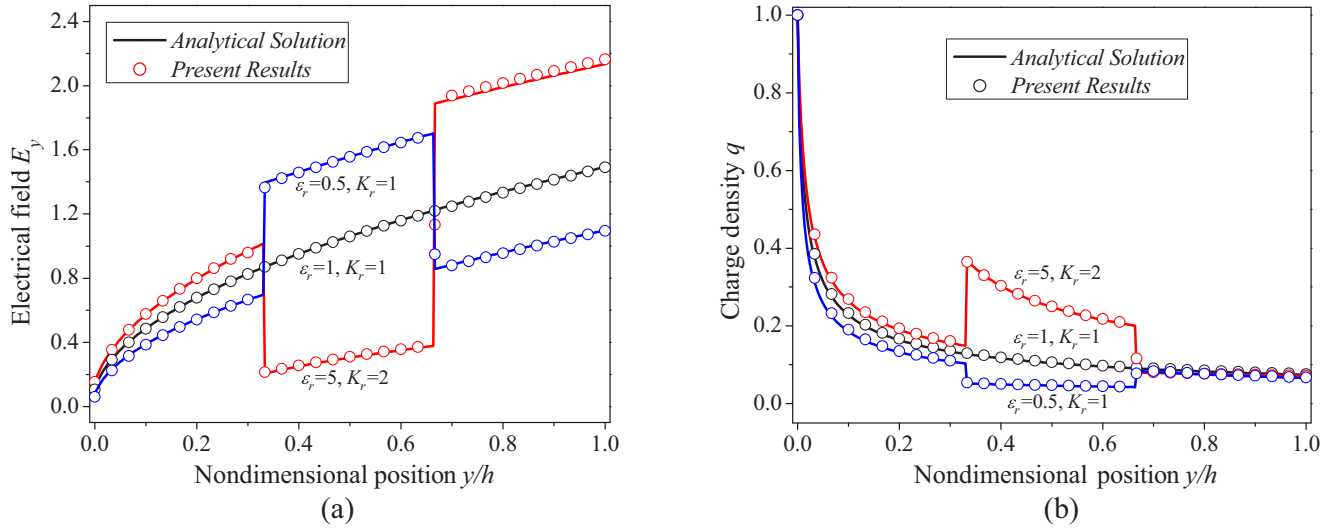


FIG. 3. Validation of the LBM model at a hydrostatic state: (a) electric field E_y and (b) charge density distributions for different combinations of permittivity ratio and mobility ratio ($\epsilon_r K_r$).

The effective number density in Eq. (18) and the Carnahan-Starling van der Waals equation of state are given, respectively, as

$$\psi = \sqrt{\frac{2(p - c_s^2 \rho)}{c_s^2 g}},$$

$$p = \rho RT \frac{1 + b\rho/4 + (b\rho/4)^2 - (b\rho/4)^3}{1 - b\rho/4} - a\rho^2, \quad (20)$$

where $a = 0.4963R^2T_c^2/p_c$ and $b = 0.18727RT_c/p_c$. The corresponding critical density ρ_c is given by $\rho_c \approx 0.5218/b$. Following Ref. [59], in our simulations we set $b = 4$, $R = 1$, $a = 0.5$, and $T_c \approx 0.047$. The effects of the parameter a will be shown in the next section.

The electrical equations, including the Poisson equation for electric potential and the Nernst-Planck equation for charge density [2], are also modeled by two lattice Boltzmann equations (LBEs). In our previous work on EHD [65], we introduced two LBEs for the electric potential and the charge

density. Some of the main formulas are expressed as

$$g_j(\mathbf{x} + \mathbf{c}_j \Delta t, t + \Delta t) - g_j(\mathbf{x}, t) = -\frac{1}{\tau_\phi} [g_j(\mathbf{x}, t) - g_j^{\text{eq}}(\mathbf{x}, t)] + \Delta t \omega_j R D_a, \quad (21)$$

$$h_j(\mathbf{x} + \mathbf{c}_j \Delta t, t + \Delta t) - h_j(\mathbf{x}, t) = -\frac{1}{\tau_q} [h_j(\mathbf{x}, t) - h_j^{\text{eq}}(\mathbf{x}, t)], \quad (22)$$

where g and h are the distribution function of the electric potential and the charge density, and τ_ϕ and τ_q are the corresponding relaxation times, respectively. \mathbf{c} , R , and D_a are the microscopic velocity, the source term, and the artificial diffusion coefficient [66], respectively. The D2Q5 velocity discretization is adopted for electric potential, while D2Q9 is used for charge density due to the convection-dominant feature of the Nernst-Planck equation. The equilibrium dis-

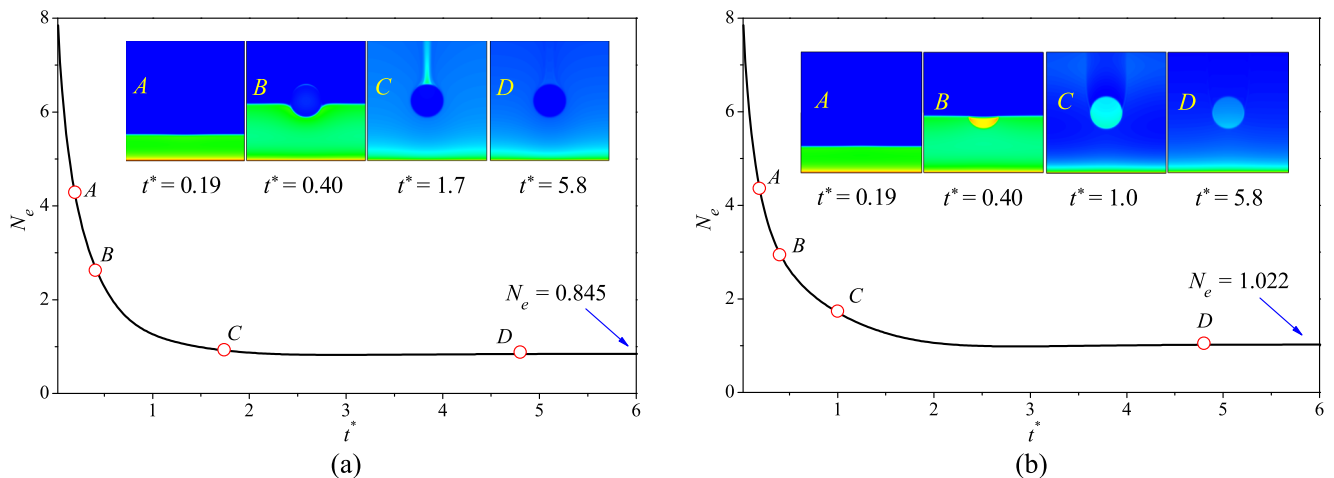


FIG. 4. Time history of electric Nusselt number N_e at hydrostatic state (a) $\epsilon_r = 0.1$, $K_r = 5$; (b) $\epsilon_r = 2$, $K_r = 1$.

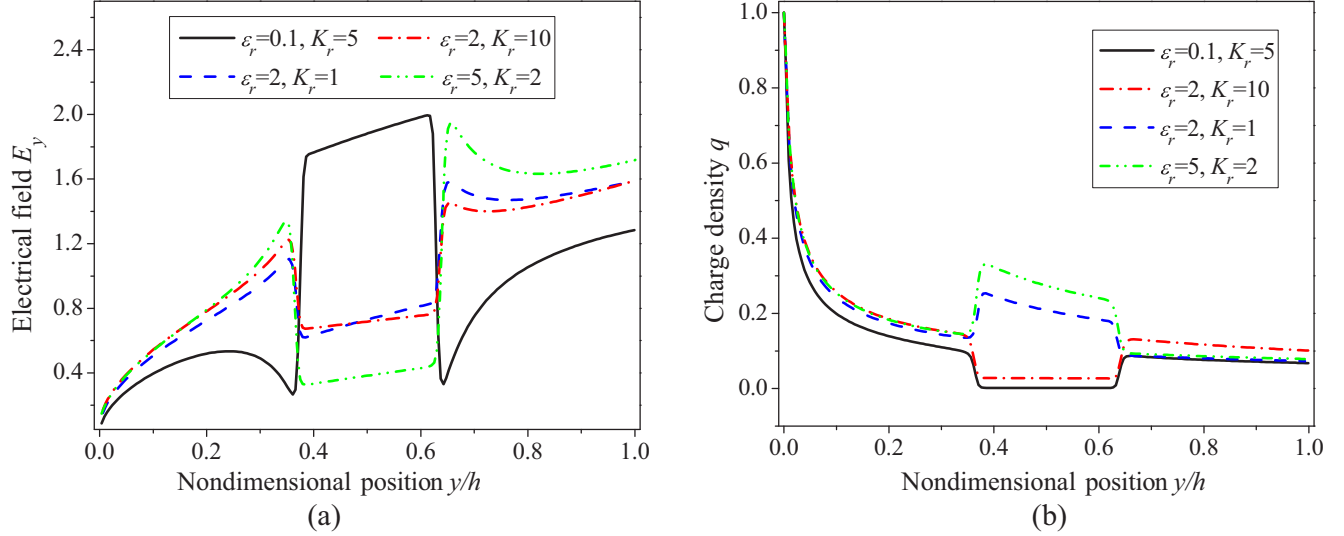


FIG. 5. (a) The electric field E_y and (b) charge density q distributions at the center line $x = L/2$ for different combinations of permittivity ratio and mobility ratio (ϵ_r, K_r) .

tribution functions g_j^{eq} and h_j^{eq} are given as

$$g_j^{\text{eq}}(\mathbf{x}, t) = \begin{cases} (\omega_0 - 1), & j = 0, \\ \omega_j \phi, & j = 1 - 4, \end{cases} \quad (23)$$

$$h_j^{\text{eq}}(\mathbf{x}, t) = q\omega_j \left\{ 1 + \frac{\mathbf{c}_j(\mathbf{K}\mathbf{E} + \mathbf{u}^p)}{c_s^2} + \frac{[\mathbf{c}_j(\mathbf{K}\mathbf{E} + \mathbf{u}^p)]^2 - c_s^2(\mathbf{K}\mathbf{E} + \mathbf{u}^p)^2}{2c_s^4} \right\}, \quad j = 1 - 9. \quad (24)$$

The corresponding weight coefficients ω and ϖ can be found in Ref. [66]. The local permittivity-dependent relaxation time τ_ϕ , the source term R , and the relaxation time τ_q can be computed from

$$\tau_\phi = \frac{\epsilon_t D_a}{\beta c^2 \Delta t} + \frac{1}{2}, \quad R = q/\epsilon, \quad \tau_q = \frac{3d}{c^2 \Delta t} + \frac{1}{2}, \quad (25)$$

where $\epsilon_t (= \epsilon/\epsilon_e)$ is the ratio between the local permittivity ϵ and the reference permittivity ϵ_e , and the artificial diffusion coefficient D_a ($D_a > 0$) is chosen to be $D_a = 1/2$ to balance the evolution speed and stability. The coefficient β has been derived to be $1/2$ by the Chapman-Enskog expansion [66]. d is the charge-diffusion coefficient. Finally, the electric potential and charge density can be evaluated as

$$\phi = \frac{1}{1 - \omega_0} \sum_{j=1}^4 g_j, \quad q = \sum_j h_j. \quad (26)$$

D. Boundary conditions and numerical implementation

As the multiphase LBM based on the diffuse-interface scheme has been adopted in this work, no special attention should be paid to the interface. The phase interface is a post-processed quantity that can be detected through monitoring the variation of the fluid densities. Therefore, the boundary condition is only required at the enclosure of the computa-

tional domain. The free boundary condition is used for all fields at the horizontal direction (left and right boundaries). As the upper and lower bound are electrodes, a nonslip boundary condition is used for the flow field and the Dirichlet boundary condition is adopted for the electric potential, while constant charge injection ($q = q_0$) is assumed at the emitter, and an outflow boundary is adopted at the receiver. At the mesoscopic level, we use the nonequilibrium extrapolation scheme [67] for the distribution functions of the electric potential. It can be expressed as [67]

$$f_j(\mathbf{r}_b, t) = f_j^{\text{eq}}(\mathbf{r}_b, t) + [f_j(\mathbf{r}_f, t) - f_j^{\text{eq}}(\mathbf{r}_f, t)], \quad (27)$$

where \mathbf{r}_b denotes the boundary lattice nodes and \mathbf{r}_f represents the nodes neighboring the boundary.

Numerical results are presented by the deformation factor $D = (L-B)/(L+B)$, where L and B are the lengths of the deformed drop in the direction parallel (y -axis) and perpendicular (x -axis) to the applied electric field, respectively. Also, by the maximum velocity magnitude as well as the electric Nusselt numbers (N_e), which is given as

$$N_e = I/I_0, \quad (28a)$$

where I is the electric current and I_0 is the single-phase hydrostatic electric current without the drop, we have

$$I = \frac{1}{L} \int_0^L \left[q(E_y + u_y) + \frac{\partial E_y}{\partial t} \right] \Big|_{y=0 \text{ or } y=1} dx, \quad (28b)$$

$$I_0 = (qE_y|_{y=0 \text{ or } y=1})_{\text{hydrostatic state}}. \quad (28c)$$

The complete solution procedure can be briefly described as follows. First, we obtain the hydrostatic solution, and we save the numerical results for further simulation. Then, we conduct the global iteration in a successive way: (i) Initialize the physical fields with the hydrostatic solution; (ii) perform the collision and streaming steps of Eq. (14), and calculate the fluid density ρ and the fluid velocity field \mathbf{u} by Eq. (17); (iii) solve the LBE for the electric potential [Eq. (21)] and calculate ϕ by Eq. (26); (iv) update the distribution of permittivity

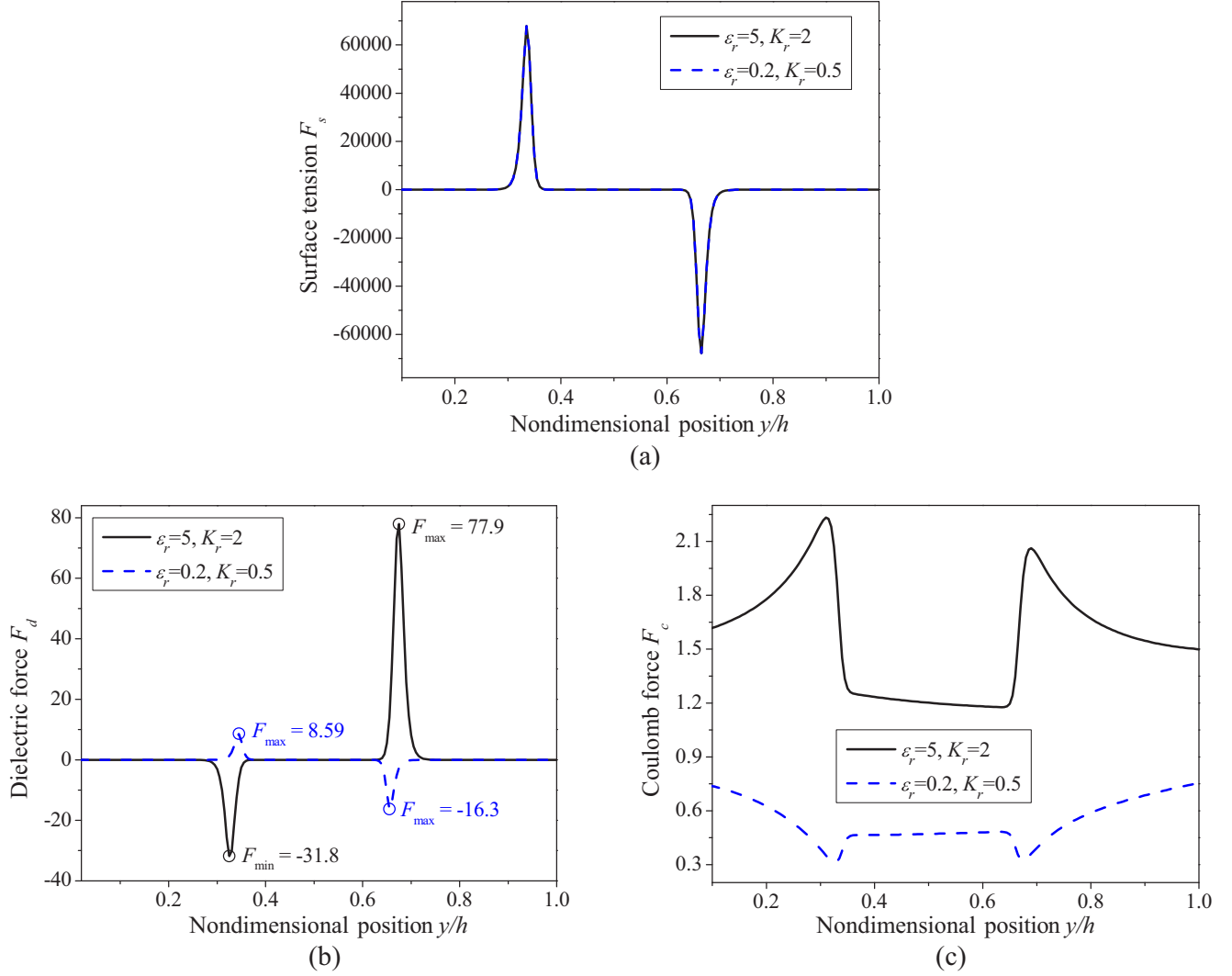


FIG. 6. Dimensionless force distributions along the vertical center line at the initial droplet motion under two typical combinations of (ϵ_r, K_r) : (a) surface tension, (b) dielectric force, and (c) Coulomb force.

ϵ and mobility K using Eq. (8), and calculate the electric field \mathbf{E} using the second-order central differencing scheme for the gradient; (v) solve the LBE for the charge density [Eq. (22)] and calculate q by Eq. (26); and (vi) go back step (ii) until the convergence criterion is satisfied.

III. RESULTS AND DISCUSSION

A. Solution at the hydrostatic state

Before investigating the multiphase EHD flow in the non-Ohmic regime, it is convenient to examine the electric field \mathbf{E} and charge density q distributions without the flow motion, known as the hydrostatic solution.

To better understand the effect of inhomogeneous permittivity ϵ and mobility K on q and \mathbf{E} distributions, we first consider a quasi-one-dimensional case by setting the drop to be a liquid layer embedded at the center of the medium ($l/3 < y_{\text{drop}} < 2l/3$). Theoretically, to maintain the continuity of the electric current and the electric displacement vector at the interface ($K_i E_i q_i = K_e E_e q_e$ and $\epsilon_i E_i = \epsilon_e E_e$), the inhomogeneous ϵ and K will induce the discontinuities of q

and \mathbf{E} distributions. We need to prove that our LBM can well reproduce this result. As provided in Appendix, we have derived the analytical solution for the quasi-one-dimensional case using the solution to the ordinary differential equations (ODEs) incorporated with the interface conditions, while numerical results are obtained using the 2D LBM code with free boundary conditions at $x = 0$ and $x = L$.

Figure 3 presents the electric field component E_y and charge density q distributions for different combinations of permittivity and mobility ratios (ϵ_r, K_r) . It is seen that the numerical results agree well with the analytical solutions, with the maximum difference less than 1%. Three representative cases with different combinations of (ϵ_r, K_r) are tested. As shown in Fig. 3 for $\epsilon_r = 1$ and $K_r = 1$, the results are the same as the single-phase hydrostatic problem. Both the electric field E_y and the charge density q show continuous distributions in the y direction. For the case $\epsilon_r = 5$ and $K_r = 2$, a sudden decrease of E_y can be observed at the interface, as shown in Fig. 3(a), with the ratio inside and outside of the drop being opposite to the permittivity ratio ϵ_r . Meanwhile, q experiences a sudden jump at the interface, and the ratio of q

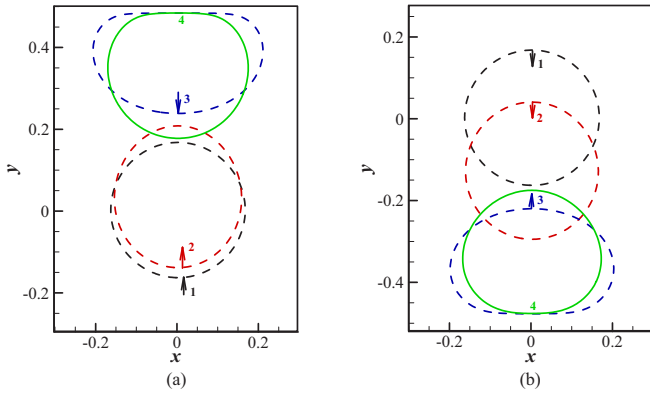


FIG. 7. The move trajectories of a drop under the combined effect of an electric field and unipolar charge injection: (a) the anode-repelled drop at $T = 200$, $Ca = 2.5$, $\epsilon_r = 5$, $K_r = 2$; and (b) the anode-attracted drop at $T = 200$, $Ca = 1.5$, $\epsilon_r = 0.2$, $K_r = 0.5$. The arrow illustrates the drop moving direction.

between the drop side and the medium side of the interface is equal to the value of $R(= \epsilon_r/K_r)$ as shown in Fig. 3(b). In the same manner, for the case $\epsilon_r = 0.5$ and $K_r = 1$, the discontinuities of E_y and q at the interface can be explained as being the corresponding permittivity and mobility differences.

Then, we consider the two-dimensional hydrostatic results. The transient evolution of the electric Nusselt number N_e calculated at the injection electrode at $\epsilon_r = 0.1$, $K_r = 5$ and $\epsilon_r = 2$, $K_r = 1$ is presented in Figs. 4(a) and 4(b), respectively. Although the time period of the charge transport is rather short, i.e., approximately the same order of magnitude as the charge relaxation time $\tau_C = \epsilon/Kq_0$, our LBM solver can well reproduce this process due to its inherent transient evolution nature. As shown in Fig. 4, the value of N_e decreases monotonically with time because the electric field next to the emitter gradually decreases as injection occurs, finally approaching the space-charge limit (SCL). The contours of charge density at four representative moments are also presented in Fig. 4. Charges are first generated in the emitter,

and then they move into the dielectric medium under the electric field (see point A in Fig. 4). Once contact is made with the drop, free charges perform differently depending on the property ratios. For $R(= \epsilon_r/K_r) < 1$, ions move faster in the drop than in the surrounding medium, which induces a “lower charge region” in the drop, and a charge plume is formed in the upper center region of the medium, as shown at point C of Fig. 4(a). On the contrary, for $R > 1$, ions move slower in the drop, resulting in a “charge-accumulated region” inside it, as shown in Fig. 4(b). In addition, the values of N_e in the steady-state case for the case $R = 0.02$ and 2 are 0.845 and 1.022, respectively, demonstrating that the existence of the “lower charge region” or the “charge-accumulated region” will decrease or increase the electric current, respectively.

The electric field E_y and charge density q distributions at the center line $x = L/2$ are presented in Fig. 5 for different permittivity and mobility ratios. The reason for the discontinuity distributions of E_y and q observed at the droplet interface is similar to that of the quasi-one-dimensional case (see Fig. 3). In addition, the value of E_y in the surrounding medium increases with an increase of ϵ_r , but an opposite trend can be found in the droplet, as shown in Fig. 5. Moreover, the value of q inside the droplet increases with an increase of R .

B. Influence of charge injection on drop dynamics

The behavior of drops under an electric field and unipolar charge injection is investigated in this section. Basic features of Ohmic LDM and non-Ohmic charge injection are analyzed comparatively. In the LDM, free charges only accumulate at the interface without bulk charges in fluid. under an electric field E_0 , electric forces at the interface will deform the drop and cause circulation patterns inside and outside the suspension droplet. However, the situation in the charge injection model is totally different. Free charges injected from the emitter will redistribute the electric field, in addition to the dielectric force at the interface, and the Coulomb force in bulk may induce complex electroconvective flows. Under that

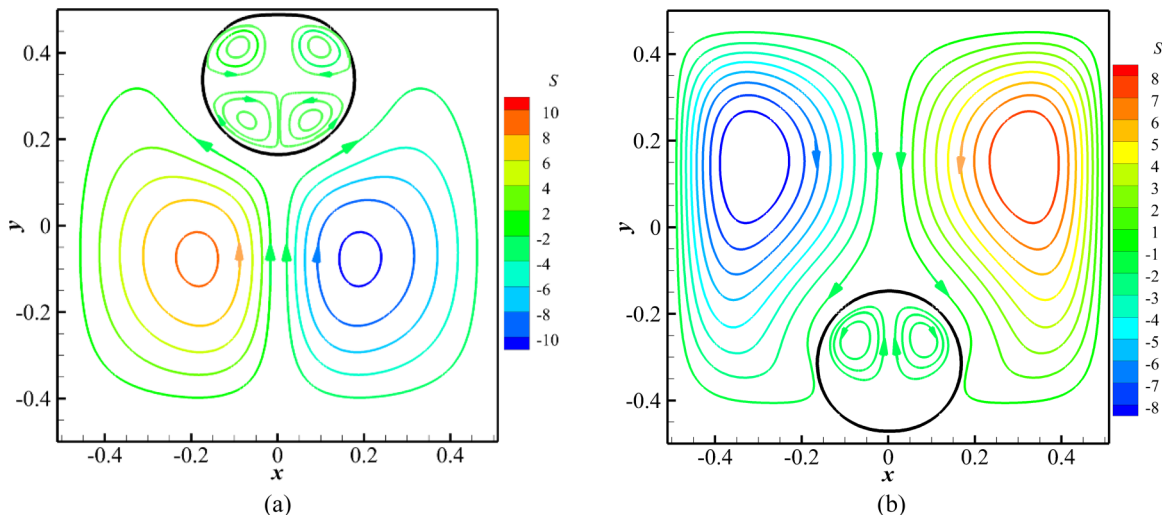


FIG. 8. Streamlines of the electroconvective flow in the medium and a secondary flow inside the drop: (a) the anode-repelled drop case at $T = 450$, $Ca = 1$, $\epsilon_r = 5$, $K_r = 2$; and (b) the anode-attracted drop at $T = 450$, $Ca = 1$, $\epsilon_r = 0.2$, $K_r = 0.5$.

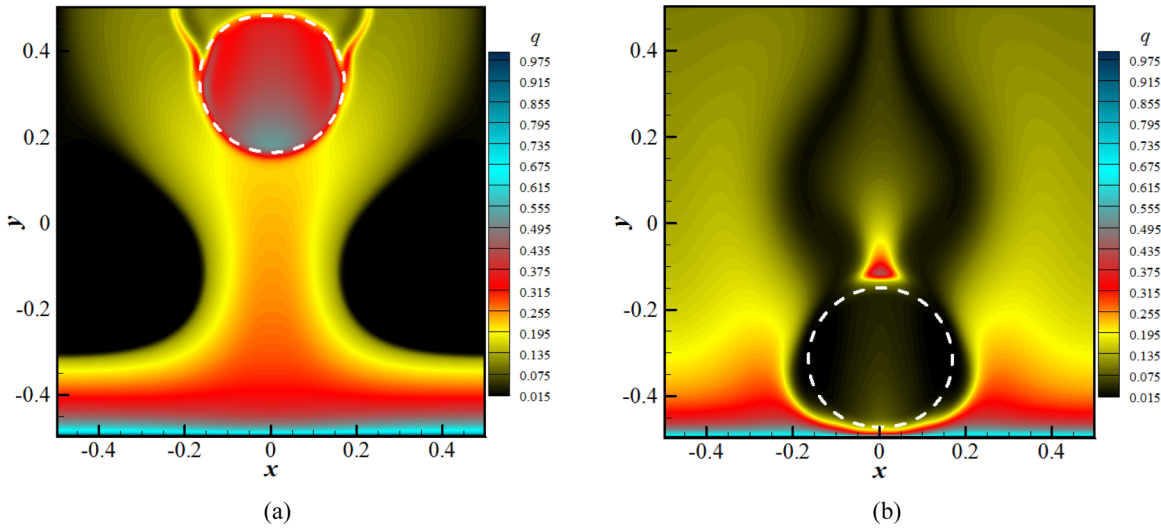


FIG. 9. Charge density distribution and the related charge void region in multiphase electrohydrodynamic flow: (a) the anode-repelled drop case at $T = 200$, $Ca = 1$, $\epsilon_r = 5$, $K_r = 2$; and (b) the anode-attracted drop at $T = 200$, $Ca = 1$, $\epsilon_r = 0.2$, $K_r = 0.5$.

condition, the drop no longer suspends in a dielectric medium but moves in a vertical direction.

Figure 6 plots the dimensionless force ($\epsilon\Delta V^2/H^3$) distributions along the vertical center line at the initial state of drop motion, corresponding to the third to fifth terms on the right side of Eq. (6b). It is seen that both surface tension F_s [Fig. 6(a)] and dielectric force F_d [Fig. 6(b)] exhibit a large gradient at several lattices close to the interface while remaining at zero in the bulk, as they are indeed surface forces but are treated as volumetric forces based on the idea of the diffusion interface method. However, the Coulomb force acts on the bulk due to the existence of volumetric free charges, as shown in Fig. 6(c). In terms of magnitude, F_s is much larger than the other two forces, but it acts on the normal direction of the interface and it will be balanced by the same magnitude of opposite force at the opposite side of the drop [see Fig. 6(a)]. In addition, the Coulomb force has a limited influence on drop behavior due to its relatively small values in this case. Therefore, the dielectric force F_d dominates the drop motion due to the inhomogeneous electric field distribution under unipolar charge injection. The unbalanced F_d at the interface results in a movement of the droplet in the fluid medium, with its direction depending on the permittivity ratio ϵ_r . For the

case $\epsilon_r > 1$, the total dielectric force has a positive direction and drives the drop moving upward, which we call an “anode-repelled drop.” On the contrary, an “anode-attracted drop” can be observed under the effect of negative dielectric force for the case $\epsilon_r < 1$.

Figure 7 shows the trajectories of both the anode-repelled drop and the anode-attracted drop under the parameters of $T = 200$, $Ca = 2.5$, $\epsilon_r = 5$, $K_r = 2$ and $T = 200$, $Ca = 1.5$, $\epsilon_r = 0.2$, $K_r = 0.5$, respectively. Interface curves are plotted at four representative moments marked by numbers 1–4 in Fig. 7. At the initial moment, the drop rapidly deforms to a prolate shape under the combined effects of electric forces and surface tension, but this prolate drop is potentially unstable due to the unbalanced dielectric force, as shown by the direction of the arrows in Fig. 7. In the accelerated moving stage, the drop becomes more deformed and loses its longitudinal symmetry due to the balance between inertia and surface tension. When the drop impacts the electrode, it is compressed to an oblate shape and then gradually becomes less deformed as the drop velocity reverses, under the assumption of the nonhydrophilic and nonlipophilic properties of the electrode and completely elastic collision. Finally, the drop may remain

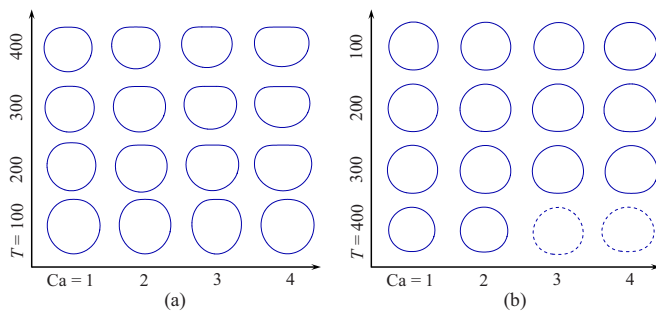


FIG. 10. Steady droplet shapes under various combinations of Ca and T : (a) anode-repelled drop at $\epsilon_r = 5$, $K_r = 2$; (b) anode-attracted droplet at $\epsilon_r = 0.2$, $K_r = 0.5$.

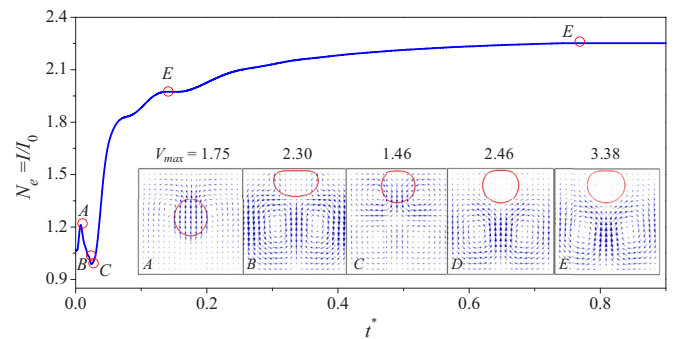


FIG. 11. Time history of N_e for the anode-repelled drop at $T = 200$ and $Ca = 2.5$. The subfigure presents the interface position and velocity vector at five representative moments.

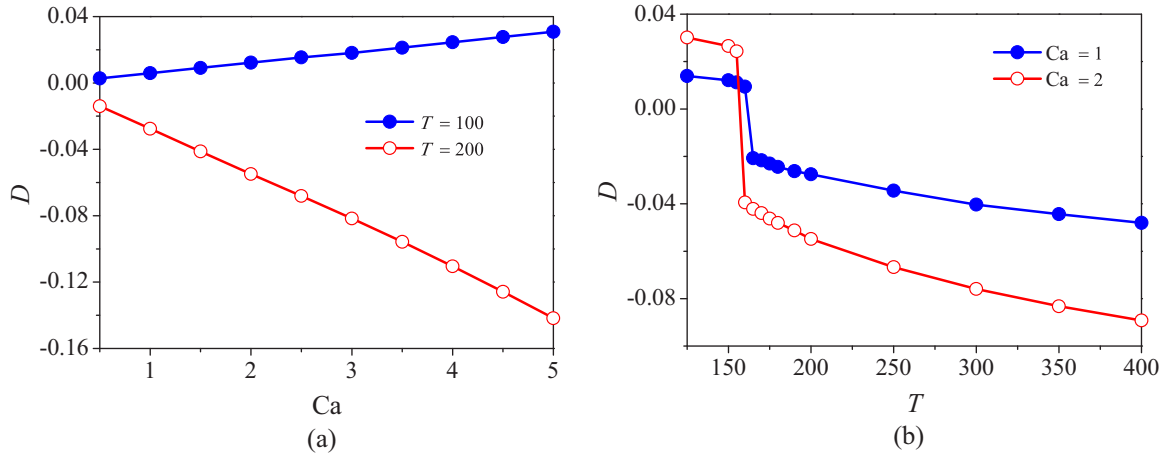


FIG. 12. The variation of drop deformation factor D with different Ca and T : (a) D - Ca curves at $T = 100$ and 200 ; (b) D - T curves at $Ca = 1$ and 2 . Other parameters considered are $\epsilon_r = 5$, $K_r = 2$, $M = 10$, and $\alpha = 10^{-4}$.

stable or start to oscillate, depending on the governing parameters.

Convective flow is one of the key features in a multiphase EHD system. In the well-known LDM, Taylor [1] reported a viscous convective flow to balance the tangential stresses provided by the action of the electric field on the interface charge; this was manifested as two pairs of symmetrical vortices. In the study of multiphase EHD in the non-Ohmic regime, convective flow can also be observed, but it is induced by a totally different mechanism. That is, for a relatively large governing parameter T , the Coulomb force exerted by the electric field on bulk free charges can overcome the viscous damping and induce a convective flow at the medium. As shown in Fig. 8, when the bulk convective flow meets the impenetrability interface, the normal component of the velocity is reduced to zero by the reactive force from the compressed oblate drop, while the tangential velocity at the interface will induce a shear stress and motivate a secondary flow inside the drop. It should be noted that the flow inside the drop is much

weaker than the bulk flow in the injection model, contrary to the situation in the LDM where the strength of the viscous flow is similar inside and outside the drop.

Figure 9 presents the charge density distributions for two representative cases $T = 200$, $Ca = 1$, $\epsilon_r = 5$, $K_r = 2$ and $T = 200$, $Ca = 1$, $\epsilon_r = 0.2$, $K_r = 0.5$. It is seen that the presence of a dielectric drop has significant effects on the bulk charge density distributions. For the anode-repelled drop in Fig. 9(a), a charge-void region can be observed on the edge of the domain, which is induced by the competition between the drift mechanism and the convection mechanism for charge transport [68]. This is also one of the representative features in single-phase electroconvective flow. In addition, the value of the charge density in the drop is obviously larger than the surrounding medium due to parameter $R > 1$, accompanied by a pair of symmetric highly charged trails that may be induced by a drag force on the drop interface. As shown in Fig. 9(b), for the anode-attracted drop, there are two low-charge regions.

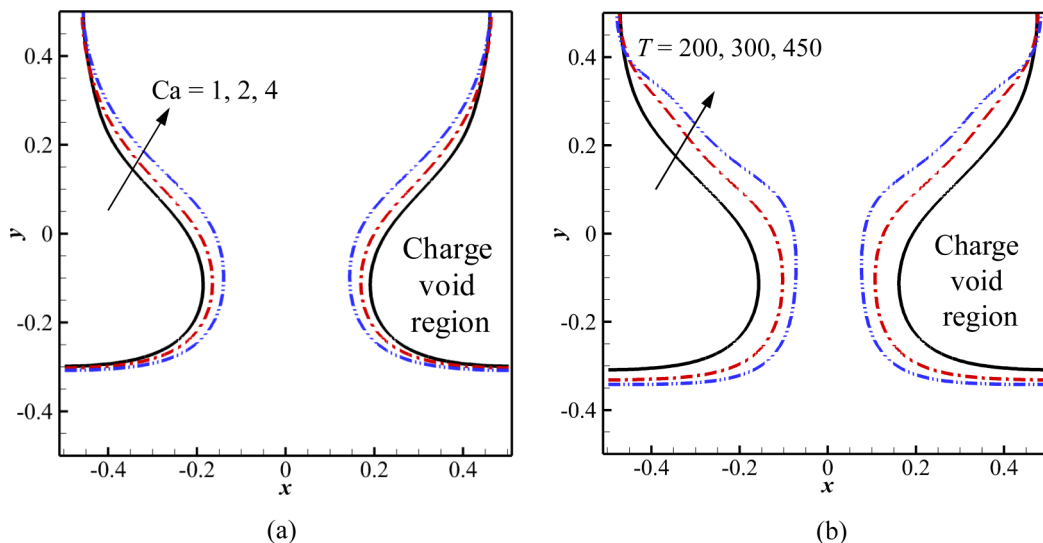


FIG. 13. The variation of the charge void region with different Ca and T : (a) different Ca at $T = 200$, (b) different T at $Ca = 1$. Here, the line of $q = 0.05$ is chosen to separate the charge void region.

One is caused by the electroconvective flow in the bulk, and the other is due to the high ion drift velocity inside the drop.

The final state shapes of the anode-repelled droplet and the anode-attracted droplet for various combinations of Ca and T are presented in Figs. 10(a) and 10(b), respectively. It is seen that drop deformation increases with both Ca and T , but their mechanisms are different. The effect of Ca on drop shape in this model is the same as that in LDM [2], that is, a larger Ca corresponds to a larger electric force or a smaller surface tension, which makes the drop easier to deform. However, the influence of T on drop shape can be explained by the fact that the stronger electroconvective flow under a larger T will induce a greater impulsive force, causing the drop to become more deformed. When the impulsive force dominates drop deformation, the drop tends to deform into an asymmetric oblate shape, also called a bowl-shaped structure.

C. Behavior of the anode-repelled droplet

In this section, we conduct a quantitative study of the transient development of the anode-repelled drop as well as its steady-state deformation. Numerical results are presented for a wide range of governing parameters T (0–500) and Ca (0–5), while the parameters of the physical properties are fixed at $\varepsilon_r = 5$, $K_r = 2$, $M = 10$, and $\alpha = 10^{-4}$.

Figure 11 plots the time history of N_e for $T = 200$ and $Ca = 2.5$. The nonmonotonic variation of N_e can be separated into several stages by five characteristic points (A, B, C, E, and F in Fig. 11). The corresponding interface position and velocity vectors are also provided. There are two mechanisms accounting for the change of N_e , namely the variation of \mathbf{E} induced by drop motion, and the change of the bulk flow velocity \mathbf{u} . The unsmooth evolution of N_e can be explained by the competition between these two mechanisms. In other words, N_e increases in the initial stage due to the perturbations in the flow field induced by the drop motion under the unbalanced dielectric force. From time A to B, the drop moves away from the emitter, leading to a decrease in the electric field, and therefore the decrease of N_e . When the drop impacts the electrode and bounces back (point B to C in Fig. 11), the drop velocity decreases first and then the drop reverses its direction, leading to decreasing fluid velocity and N_e . After time C, the situation gets simpler as the drop no longer changes position. Electroconvective flow becomes more developed in this period, and both the maximum velocity V_{\max} and N_e increase as time goes on. In addition, stronger electroconvection in the bulk will impose a larger impulsive force on the interface, and it will cause the drop to deform more to an oblate shape. Finally, the drop will steadily attach to the upper electrode under the combined effect of electric force and impulsive force from the electroconvective flow.

The linear relation between D and Ca at small values of Ca is a key characteristic of drop deformation under an electric field. For the classic LDM, a linear expression $D = F(\varepsilon_r, \sigma_r)Ca$ has been obtained by Feng [6] based on the first-order small-deformation model. Simulations based on different numerical methods have also reproduced this linear relationship [41,42]. In this section, we seek out similar relationships between D and Ca and T in the non-Ohmic regime. Figure 12(a) presents the D - Ca curves at $T = 100$

and 200, and linear trends can be observed in both cases. For $T = 100$, the electroconvective flow has not been motivated (the linear stability criterion of single-phase electroconvection is $T_c = 164.1$ [23,28]). The mechanism of drop deformation is similar to that of LDM [2], that is, under the combined effect of surface forces, the drop deforms into a prolate shape due to the dominant dielectric force. However, for $T = 200$, the situation is totally different as bulk convective flow has been fully developed and starts to dominate the drop deformation. As a consequence, an impulsive force is imposed on the bottom of the drop and compresses it into a bowl shape, as shown in Fig. 11. Although a linear relationship between D and Ca can be observed for both prolate-shaped and bowl-shaped drops, their slopes are different due to the different dominant mechanisms of drop deformation. The calculated slopes of D - Ca curves at $T = 100$ and 200 are 0.00621 and -0.0281 , respectively, which means the presence of bulk electroconvective flow changes not only the magnitude of drop deformation, but also its direction.

The relationship between D and T is more complex. As shown in Fig. 12(b), the value of D decreases monotonously along with increasing T because a strong impulsive force under a high T tends to compress the drop into an oblate shape. A sudden decrease of D can be observed at the linear stability criterion T_c where the bulk electroconvective flow has been motivated. Due to the subcritical bifurcation of electroconvective flow, when T exceeds T_c , the bulk velocity jumps from zero to a finite amplitude value, leading to the sharp decrease of D . On the other hand, when compared to the single-phase electroconvection model between two plate electrodes, the presence of a drop in the multiphase model has some effects on T_c . Quantificationally, the values of T_c in the cases $Ca = 1$ and 2 are approximately estimated to be 162.5 and 157.5, respectively, which is lower than the value of the single phase (164.1) [23,28].

In Fig. 13 we have displayed the curve $q = 0.05$, which materializes the boundary between the charged and non-charged regions at different Ca and T . The value of q in the charge-void region is not strictly zero but is fairly small, of order 10^{-5} – 10^{-4} . This is due to the charge diffusion considered in this work. As shown in Fig. 13(a), the size of the void region

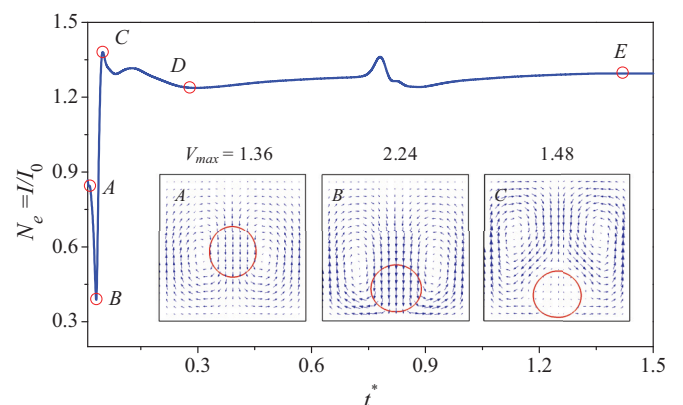


FIG. 14. Time history of N_e for the anode-attracted drop at $T = 200$ and $Ca = 2.5$. Other parameters considered are $\varepsilon_r = 0.2$, $K_r = 0.5$, $M = 10$, and $\alpha = 10^{-4}$.

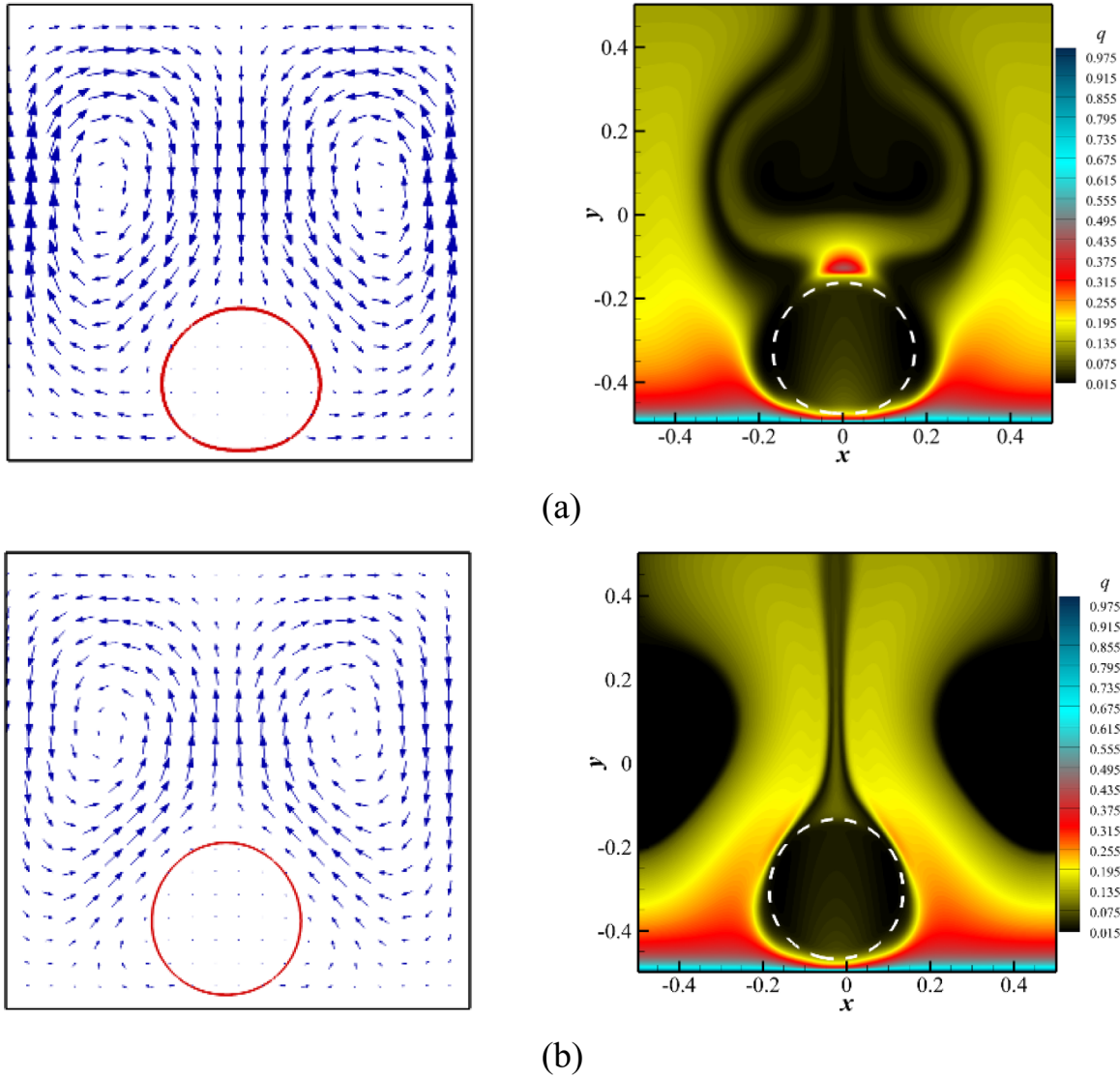


FIG. 15. Velocity vector and charge density distribution of two possible states of the anode-attracted drop: (a) quasisteady centrally downward flow corresponding to point *E* in Fig. 14, (b) centrally upward flow corresponding to point *F* in Fig. 14.

increases slightly as *Ca* increases. This can be explained by the fact that a larger *Ca* corresponds to a more oblate deformed drop and stronger bulk flow. In addition, the charge-void region increases significantly with increasing *T*, as the values of *T* are directly related to the flow strength.

D. Behavior of the anode-attracted droplet

In this section, we study the transient motion and steady deformation of the anode-attracted drop. As discussed in Sec. IV B, drop settling is mainly induced by the downward net force imposed by the electric field on the interface. In numerical simulation, we focus on the effects of *T* and *Ca*, with physical property parameters being fixed at $\epsilon_r = 0.2$, $K_r = 0.5$, $M = 10$, and $\alpha = 10^{-4}$.

Figure 14 presents the transient development of electric Nusselt number N_e for $T = 200$ and $Ca = 2.5$. Drop interface and velocity vector are also provided in Fig. 14. The mechanism for the variation of N_e is the same as that in the

anode-repelled drop case, that is, a competition between drop motion and bulk convective flow. In the period when the drop moves downward to the emitter (*A-B* in Fig. 14), the velocity magnitude increases in the $-y$ direction and the effective electric potential decreases, leading to a decrease of N_e . When the drop impacts the emitter, the drop velocity decreases to zero. At the same time, bulk convective flow starts to develop, resulting in an increase of Nu (*B-C* in Fig. 14). During stage *C-E*, the system evolves into a quasisteady state, in which the drop is compressed to an oblate shape by a center-downward electroconvective flow. However, the quasisteady state at time point *E* is potentially unstable, and the system will transfer to a more stable state marked by *F* in Fig. 14 after a long evolution time. To explain the mechanism of flow transition, in Fig. 15 we have plotted both the flow field and the charge density distribution at time points *E* and *F*. A centrally downward flow can be observed in Fig. 15(a), i.e., fluid descends in the center of the domain, hits the drop surface, and then ascends at the peripheral region. A corresponding charge void

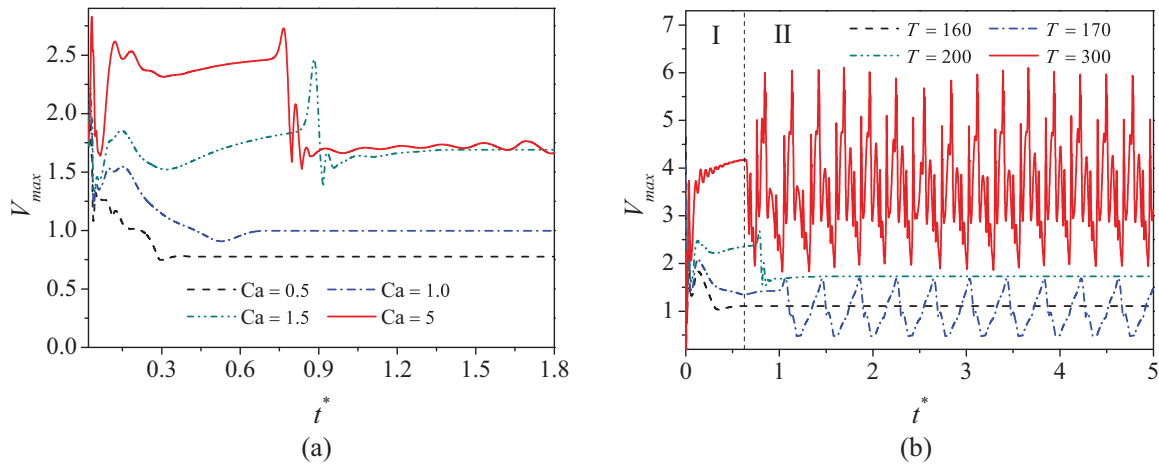


FIG. 16. Time history of V_{max} under different governing parameters Ca and T : (a) evolution of electroconvective flow with the increasing of Ca at $T = 200$, and (b) flow transitions as T increases at $Ca = 4$. Other parameters considered are $\epsilon_r = 0.2$, $K_r = 0.5$, $M = 10$, and $\alpha = 10^{-4}$.

region is formed above the drop due to the equilibrium of inertia force and Coulomb repulsive force. However, this unstable equilibrium will be broken when the convective flow strength exceeds the limitations of Coulomb repulsion. Therefore, the system will finally transfer to a centrally upward flow with a charge void region at the edge of the domain, as presented in Fig. 15(b).

Flow transition and the related instability with increasing governing parameters Ca and T are briefly discussed in this part. In Fig. 16(a), the evolution of maximum velocity V_{max} is presented for different Ca at $T = 200$. For relatively small values of Ca ($= 0.5$ and 1.0), a stable centrally downward flow [see Fig. 15(a)] can be observed. With increasing Ca , strong convective flow breaks the original equilibrium, resulting in a transition of the system into another steady centrally upward pattern [see Fig. 15(b)]. Upon further increasing the parameter Ca to 5, a slight swing of the drop occurs in the horizontal direction, leading to a periodic change of V_{max} as shown in Fig. 16(a). By fixing $Ca = 4$ and changing T , we can obtain another route of the transition of flow. In the previous numerical study of Wang *et al.* [69] for single-phase electroconvective flow induced by unipolar injection,

the system continually experiences the hydrostatic state ($T < 164$), steady flow ($164 < T < 213$), periodic flow ($213 < T < 281$), second steady flow ($281 < T < 419$), oscillatory flow, and finally becomes chaotic with the increase of T . Obviously, the situation is more complex in the presence of the anode-attracted drop. As illustrated in Fig. 16(b), the transient development of the flow can be simply separated into two stages, marked by I and II in Fig. 16(b), respectively. The system first develops a centrally downward flow in stage I due to the downward motion of the drop, and then it evolves into different flow styles depending on T at stage II. At a relatively small $T = 160$, the system will keep the centrally downward pattern at stage II, but this steady state is potentially unstable at larger T ($= 170$), where the drop periodically swings in the horizontal direction, leading to a periodic flow as shown in Fig. 16(b). With a further increase of T ($= 200$), a transition from a centrally downward flow to a steady upward flow can be obtained. At $T = 300$, centrally upward flow is no longer stable and the system evolves into an oscillation state. In conclusion, when T varies from 160 to 300, this multiphase EHD case successively experiences steady flow, periodic flow, second steady flow, and oscillatory flow.

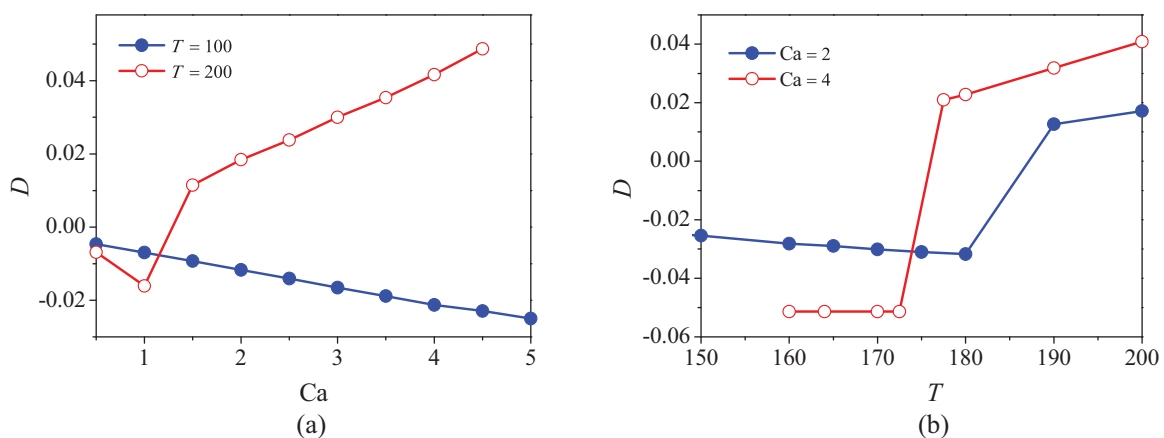


FIG. 17. The variation of D with different Ca and T for the anode-attracted drop: (a) D - Ca curves at $T = 100$ and 200; (b) D - T curves at $Ca = 2$ and 4. Other parameters considered are $\epsilon_r = 0.2$, $K_r = 0.5$, $M = 10$, and $\alpha = 10^{-4}$.

The variations of deformation factor D under different Ca and T are presented in Fig. 17. It can be observed that the D - Ca curve has an approximately linear relationship. For $T = 100$, the bulk convective flow has not been well developed, and drop deformation is dominated by the unbalanced dielectric force on the interface, therefore the value of D decreases with an increase of Ca , as shown in Fig. 17(a). But for $T = 200$, the value of D experiences a sharp increase, at which point the drop shape changes from oblate to prolate due to the flow transition from centrally downward flow to upward flow. As illustrated in Fig. 17(b), the D - T curves at $Ca = 2$ and 4 share a similar trend, that is, the value of D first decreases linearly, then jumps to a positive value due to the flow transition, and then increases linearly as T increases.

IV. CONCLUSIONS

In the present work, the study of multiphase EHD is extended to the non-Ohmic conduction regime. A fundamental case of drop deformation under the simultaneous action of unipolar charge injection and electric field is investigated. Direct numerical simulation based on fully coupled equations is performed based on our recently developed unified lattice Boltzmann model. Numerical results are presented for both the transient drop motion and steady-state deformation, and several key conclusions can be drawn as follows:

(i) At the hydrostatic state without flow motion, an analytical solution is derived for a quasi-one-dimensional case, and the numerical results agree well with the analytical solutions, with a maximum difference less than 1%. A discontinuity can be observed in the E_y and q distributions due to the different physical properties inside and outside of the drop. Specifically, the ratios of E_y at different sides of the interface are inversely proportional to the permittivity ratio ϵ_r , while the ratio of q is equal to the value of $R(= \epsilon_r/K_r)$. For $R < 1$, ions move faster in the drop than in the surrounding medium, which induces a “lower charge region” and a relatively small electric Nusselt number N_e . For $R > 1$, however, ions move slower in the drop, resulting in a “charge-accumulated region” inside the drop and a larger N_e than in the single-phase results.

(ii) Unlike the steady suspension droplet in the well-known leaky dielectric model (LDM), unsteady drop motion will be motivated due to the unbalanced electric force in the injection model. For the cases considered in this paper, the net dielectric force at the interface dominates the flow, and the drop motion depends on the permittivity ratio ϵ_r . In detail, at $\epsilon_r > 1$ the drop moves in an upward direction to the receiver electrode, referred to as the “anode-repelled drop.” On the contrary, the “anode-attracted drop” can be observed under the effect of negative dielectric force for the case $\epsilon_r < 1$. In addition, a bulk electroconvective flow will be induced by the volumetric free charge under the electric field, and a secondary flow can also be observed inside the drop due to the viscous shear force at the interface induced by the tangential motion of yj surrounding medium.

(iii) For the anode-repelled case, the drop experiences an accelerated upward motion, collision with the electrode, and then a bounce-back, finally deforming into a “bowl-shaped

structure” (an asymmetric oblate shape). An interesting feature found in the present study is that the deformation factor D maintains a linear relationship with Ca in the presence of bulk flow. Quantificationally, the calculated slopes of D - Ca curves at $T = 100$ and 200 are 0.00621 and -0.0281 , respectively, which means that the presence of bulk electroconvective flow changes not only the magnitude of drop deformation, but also its direction. However, the D - T relationship is more complex due to the subcritical bifurcation of electroconvection. A sudden decrease of D can be observed at the linear stability criterion T_c where the bulk electroconvective flow has been motivated. On the other hand, the presence of a drop makes the bulk flow easier to motivate than the single-phase problem, reflected in the decreasing values of T_c to 157.5 , which is lower than the value of the single phase (164.1).

(iv) For the anode-attracted drop, the system first evolves into a quasisteady state where the drop is compressed into an oblate shape by a center-downward electroconvective flow, and then it develops into different flow styles depending on T . With T varying from 160 to 300 , this multiphase EHD case successively experiences steady flow, periodic flow, second steady flow, and oscillatory flow. In addition, variations of the deformation factor D under different Ca and T have a basic linear relationship, but discontinuities can be observed in D - Ca and D - T curves due to the flow transition from centrally downward flow to upward flow.

ACKNOWLEDGMENTS

This work is supported by the National Natural Science Foundation of China (Grants No. 51906051 and No. 52076055), and the Fundamental Research Funds for the Central Universities (Grant No. AUEAS750303121).

APPENDIX: DERIVATION OF ANALYTICAL SOLUTIONS

We have the electric part equation for the charge injection model, including the Gauss law for the electric field (\mathbf{E}) in Eq. (A1) and the charge and Nernst-Planck equation for the conservation of charge density in Eq. (A2),

$$\nabla \cdot \epsilon \mathbf{E} = q, \quad (\text{A1})$$

$$\frac{\partial q}{\partial t} + \mathbf{u} \cdot \nabla q = \nabla \cdot (-Kq\mathbf{E} + D\nabla q). \quad (\text{A2})$$

For the hydrostatic solution at steady state and neglecting charge diffusion, we need to solve the following simplified equations:

$$\nabla \cdot \epsilon \mathbf{E} = q, \quad \nabla \cdot (Kq\mathbf{E}) = 0. \quad (\text{A3})$$

Equations (A3) are ordinary differential equations. Their general solution in the one-dimensional case can be obtained as

$$\begin{aligned} \mathbf{E} &= a(z+b)^{1/2}, \quad q = \frac{a\epsilon}{2(z+b)^{1/2}}, \\ \phi &= -\frac{2}{3}a(z+b)^{3/2} + c, \end{aligned} \quad (\text{A4})$$

where a , b , and c are constants to be determined. In addition, the values of a , b , and c are different in different layers, labeled by the subscripts 1–3 in layers 1–3, respectively.

Combined with the conditions at the boundaries and interfaces, we have the following: at $z = 0$, $q = C$, $\phi = 1$; at $z = 1/3$, $K_r q_2 E z_2 = q_1 E z_1$, $\varepsilon_r E z_2 = E z_1$; at $z = 2/3$, $K_r q_2 E z_2 = q_3 E z_3$, $\varepsilon_r E z_2 = E z_3$, where ε_r and K_r are the permittivity and mobility ratios between dielectric 2 and dielectric 1.

We have the following coupled algebraic equations:

$$a_1 = 2C b_1^{1/2}, \quad a_2 = \frac{1}{\sqrt{\varepsilon_r K_r}} a_1, \quad a_3 = a_1, \quad b_2 = \frac{K_r}{\varepsilon_r} \left(b_1 + \frac{1}{3} \right) - \frac{1}{3}, \quad b_3 = b_1 + \frac{\varepsilon_r}{3K_r} - \frac{1}{3},$$

$$\frac{2}{3} a_1 \left[\left(\frac{1}{3} + b_1 \right)^2 - b_1^{3/2} \right] + \frac{2}{3} a_2 \left[\left(\frac{2}{3} + b_2 \right)^2 - \left(\frac{1}{3} + b_2 \right)^2 \right] + \frac{2}{3} a_3 \left[(1 + b_3)^2 - \left(\frac{2}{3} + b_3 \right)^2 \right] - 1 = 0.$$

-
- [1] J. R. Melcher and G. I. Taylor, Electrohydrodynamics: a review of the role of interfacial shear stresses, *Annu. Rev. Fluid Mech.* **1**, 111 (1969).
- [2] D. A. Saville, Electrohydrodynamics: the Taylor-Melcher leaky dielectric model, *Annu. Rev. Fluid Mech.* **29**, 27 (1997).
- [3] O. Vizika and D. A. Saville, The electrohydrodynamic deformation of drops suspended in liquids in steady and oscillatory electric fields, *J. Fluid Mech.* **239**, 1 (1992).
- [4] T. Tsukada, T. Katayama, Y. Ito, and M. Hozawa, Theoretical and experimental studies of circulations inside and outside a deformed drop under a uniform electric field, *J. Chem. Eng. Jpn.* **26**, 698 (1993).
- [5] J. A. Lanauze, L. M. Walker, and A. S. Khair, Nonlinear electrohydrodynamics of slightly deformed oblate drops, *J. Fluid Mech.* **774**, 245 (2015).
- [6] J. Q. Feng, A 2D electrohydrodynamic model for electrorotation of fluid drops, *J. Colloid Interface Sci.* **246**, 112 (2002).
- [7] J. Zhang and D. Y. Kwok, A 2D lattice Boltzmann study on electrohydrodynamic drop deformation with the leaky dielectric theory, *J. Comput. Phys.* **206**, 150 (2005).
- [8] J. Q. Feng and T. C. Scott, A computational analysis of electrohydrodynamics of a leaky dielectric drop in an electric field, *J. Fluid Mech.* **311**, 289 (2006).
- [9] G. Supene, C. R. Koch, and S. Bhattacharjee, Deformation of a droplet in an electric field: nonlinear transient response in perfect and leaky dielectric media, *J. Colloid Interface Sci.* **318**, 463 (2008).
- [10] J. M. López-Herrera, S. Popinet, and M. A. Herrada, A charge-conservative approach for simulating electrohydrodynamic two-phase flows using volume-of-fluid, *J. Comput. Phys.* **230**, 1939 (2011).
- [11] Z. T. Li, G. J. Li, H. B. Huang, and X. Y. Lu, Lattice Boltzmann study of electrohydrodynamic drop deformation with large density ratio, *Int. J. Mod. Phys. C* **22**, 729 (2011).
- [12] Y. Lin, P. Skjetne, and A. Carlson, A phase field model for multiphase electrohydrodynamic flow, *Int. J. Multiphase Flow* **45**, 1 (2012).
- [13] O. Schnitzer and E. Yariv, The Taylor-Melcher leaky dielectric model as a macroscale electrokinetic description, *J. Fluid Mech.* **773**, 1 (2015).
- [14] D. Das and D. Saintillan, A nonlinear small-deformation theory for transient droplet electrohydrodynamics, *J. Fluid Mech.* **810**, 225 (2016).
- [15] R. Singh, S. S. Bahga, and A. Gupta, Electrohydrodynamics in leaky dielectric fluids using lattice Boltzmann method, *Eur. J. Mech. B Fluids* **74**, 167 (2019).
- [16] C. Sorgentone, A. K. Tornberg, and P. M. Vlahovska, A 3D boundary integral method for the electrohydrodynamics of surfactant-covered drops, *J. Comput. Phys.* **389**, 111 (2019).
- [17] M. Pan, D. He, and K. Pan, Energy stable finite element method for an electrohydrodynamic model with variable density, *J. Comput. Phys.* **424**, 109870 (2021).
- [18] F. M. J. McCluskey, P. Atten, and A. T. Perez, Heat transfer enhancement by electroconvection resulting from an injected space charge between parallel plates, *Int. J. Heat Mass Transf.* **34**, 2237 (1991).
- [19] P. Traoré and J. Wu, On the limitation of imposed velocity field strategy for Coulomb-driven electroconvection flow simulations, *J. Fluid Mech.* **727**, R3 (2013).
- [20] W. Hassen, M. I. Elkhazen, P. Traore, and M. N. Borjini, Numerical study of the electro-thermo-convection in an annular dielectric layer subjected to a partial unipolar injection, *Int. J. Heat Fluid Flow* **50**, 201 (2014).
- [21] J. Wu, P. A. Vázquez, P. Traoré, and A. T. Pérez, Finite amplitude electroconvection induced by strong unipolar injection between two coaxial cylinders, *Phys. Fluids* **26**, 124105 (2014).
- [22] M. Zhang, F. Martinelli, J. Wu, P. J. Schmid, and M. Quadrio, Modal and non-modal stability analysis of electrohydrodynamic flow with and without cross-flow, *J. Fluid Mech.* **770**, 319 (2015).
- [23] M. Zhang, Weakly nonlinear stability analysis of subcritical electrohydrodynamic flow subject to strong unipolar injection, *J. Fluid Mech.* **792**, 328 (2016).
- [24] Y. Guan and I. Novosselov, Two relaxation time lattice Boltzmann method coupled to fast Fourier transform Poisson solver: application to electroconvective flow, *J. Comput. Phys.* **397**, 108830 (2019).
- [25] K. Luo, J. Wu, H.-L. Yi, L. H. Liu, and H.-P. Tan, Hexagonal convection patterns and their evolutionary scenarios in electroconvection induced by a strong unipolar injection, *Phys. Rev. Fluids* **3**, 053702 (2018).
- [26] K. Luo, J. Wu, H.-L. Yi, and H.-P. Tan, Three-dimensional finite amplitude electroconvection in dielectric liquids, *Phys. Fluids* **30**, 023602 (2018).
- [27] Y. Guan, J. Riley, and I. Novosselov, Three-dimensional electroconvective vortices in cross flow, *Phys. Rev. E* **101**, 033103 (2020).
- [28] J. C. Lacroix, P. Atten, and E. J. Hopfinger, Electro-convection in a dielectric liquid layer subjected to unipolar injection, *J. Fluid Mech.* **69**, 539 (1975).

- [29] F. Pontiga, A. Castellanos, and B. Malraison, Some considerations on the instabilities of nonpolar liquids subjected to charge injection, *Phys. Fluids* **7**, 1348 (1995).
- [30] D. Testi, Heat transfer enhancement by an impinging ionic jet in a viscous transformer coolant, *Int. Commun. Heat Mass Transf.* **91**, 256 (2018).
- [31] A. Castellanos and P. Atten, Numerical modeling of finite amplitude convection of liquids subjected to unipolar injection, *IEEE Trans. Ind. Appl.* **IA-23**, 825 (1987).
- [32] P. A. Vázquez and A. Castellanos, Numerical simulation of EHD flows using discontinuous galerkin finite element methods, *Comput. Fluids* **84**, 270 (2013).
- [33] P. H. Traoré, A. T. Pérez, D. Koulova, and H. Romat, Numerical modelling of finite-amplitude electro-thermo-convection in a dielectric liquid layer subjected to both unipolar injection and temperature gradient, *J. Fluid Mech.* **658**, 279 (2010).
- [34] D. D. Hong, J. S. Wang, G. R. Liu, Y. Z. Chen, J. Han, and N. G. Hadjiconstantinou, Dissipative particle dynamics simulations of electroosmotic flow in nano-fluidic devices, *Microfluid. Nanofluid.* **4**, 219 (2008).
- [35] M. Wang and Q. Kang, Modeling electrokinetic flows in microchannels using coupled lattice boltzmann methods, *J. Comput. Phys.* **229**, 728 (2010).
- [36] L. Wang, Z. Wei, T. Li, Z. Chai, and B. Shi, A lattice boltzmann modelling of electrohydrodynamic conduction phenomenon in dielectric liquids, *Appl. Math. Modell.* **95**, 361 (2021).
- [37] K. Luo, J. Wu, H.-L. Yi, and H.-P. Tan, Lattice boltzmann model for Coulomb-driven flows in dielectric liquids, *Phys. Rev. E* **93**, 023309 (2016).
- [38] K. Luo, J. Wu, H.-L. Yi, and H.-P. Tan, Lattice boltzmann modelling of electro-thermo-convection in a planar layer of dielectric liquid subjected to unipolar injection and thermal gradient, *Int. J. Heat Mass Transf.* **103**, 832 (2016).
- [39] K. Luo, A. T. Pérez, J. Wu, H.-L. Yi, and H.-P. Tan, Efficient lattice boltzmann method for electrohydrodynamic solid-liquid phase change, *Phys. Rev. E* **100**, 013306 (2019).
- [40] N. Felici and J. C. Lacroix, Electroconvection in insulating liquids with special reference to uni- and bi-polar injection, *J. Electrostat.* **5**, 135 (1978).
- [41] Y. Cui, N. Wang, and H. Liu, Numerical study of droplet dynamics in a steady electric field using a hybrid lattice boltzmann and finite volume method, *Phys. Fluids* **31**, 022105 (2019).
- [42] X. Liu, Z. Chai, and B. Shi, A phase-field-based lattice boltzmann modeling of two-phase electro-hydrodynamic flows, *Phys. Fluids* **31**, 092103 (2019).
- [43] P. Atten, Electrohydrodynamic instability and motion induced by injected space charge in insulating liquids, dielectrics and electrical insulation, *IEEE Trans.* **3**, 1 (1996).
- [44] D. M. Anderson, G. B. McFadden, and A. A. Wheeler, Diffuse-interface methods in fluid mechanics, *Annu. Rev. Fluid Mech.* **30**, 139 (1998).
- [45] A. T. Pérez and A. Castellanos, Role of charge diffusion in finite-amplitude electroconvection, *Phys. Rev. A* **40**, 5844 (1989).
- [46] C. K. Aidun and J. R. Clausen, Lattice-Boltzmann method for complex flows, *Annu. Rev. Fluid Mech.* **42**, 439 (2010).
- [47] Q. Li, K. H. Luo, Q. J. Kang, Y. L. He, Q. Chen, and Q. Liu, Lattice boltzmann methods for multiphase flow and phase-change heat transfer, *Prog. Energy Combust. Sci.* **52**, 62 (2016).
- [48] L. S. Luo and S. S. Girimaji, Theory of the lattice boltzmann method: Two-fluid model for binary mixtures, *Phys. Rev. E* **67**, 036302 (2003).
- [49] A. Fakhari, M. Geier, and T. Lee, A mass-conserving lattice boltzmann method with dynamic grid refinement for immiscible two-phase flows, *J. Comput. Phys.* **315**, 434 (2016).
- [50] X. Shan and H. Chen, Lattice boltzmann model for simulating flows with multiple phases and components, *Phys. Rev. E* **47**, 1815 (1993).
- [51] P. Yuan and L. Schaefer, Equations of state in a lattice boltzmann model, *Phys. Fluids* **18**, 042101 (2006).
- [52] Q. Li and K. H. Luo, Effect of the forcing term in the pseudopotential lattice boltzmann modeling of thermal flows, *Phys. Rev. E* **89**, 053022 (2014).
- [53] Q. Li, K. H. Luo, Q. J. Kang, and Q. Chen, Contact angles in the pseudopotential lattice boltzmann modeling of wetting, *Phys. Rev. E* **90**, 053301 (2014).
- [54] H. Liu, A. J. Valocchi, and Q. Kang, Three-dimensional lattice boltzmann model for immiscible two-phase flow simulations, *Phys. Rev. E* **85**, 046309 (2012).
- [55] C. M. Pooley and K. Furtado, Eliminating spurious velocities in the free-energy lattice boltzmann method, *Phys. Rev. E* **77**, 046702 (2008).
- [56] G. H. Tang, H. H. Xia, and Y. Shi, Study of wetting and spontaneous motion of droplets on microstructured surfaces with the lattice boltzmann method, *J. Appl. Phys.* **117**, 244902 (2015).
- [57] H. W. Zheng, C. Shu, and Y. T. Chew, A lattice boltzmann model for multiphase flows with large density ratio, *J. Comput. Phys.* **218**, 353 (2006).
- [58] E. D. Kumar, S. A. Sannasiraj, and V. Sundar, Phase field lattice boltzmann model for air-water two phase flows, *Phys. Fluids* **31**, 072103 (2019).
- [59] Q. Li, K. H. Luo, and X. J. Li, Lattice boltzmann modeling of multiphase flows at large density ratio with an improved pseudopotential model, *Phys. Rev. E* **87**, 053301 (2013).
- [60] L. Chen, Q. Kang, Y. Mu, Y. L. He, and W. Q. Tao, A critical review of the pseudopotential multiphase lattice boltzmann model: methods and applications, *Int. J. Heat Mass Transf.* **76**, 210 (2014).
- [61] S. Chen and G. D. Doolen, Lattice boltzmann method for fluid flows, *Annu. Rev. Fluid Mech.* **30**, 329 (1998).
- [62] X. He and L. S. Luo, Theory of the lattice boltzmann method: from the boltzmann equation to the lattice boltzmann equation, *Phys. Rev. E* **56**, 6811 (1997).
- [63] Z. Guo, C. Zheng, and B. Shi, Discrete lattice effects on the forcing term in the lattice boltzmann method, *Phys. Rev. E* **65**, 046308 (2002).
- [64] A. Castellanos, *Electrohydrodynamics* (Springer, New York, 1998), Vol. 380.
- [65] K. Luo, J. Wu, H.-L. Yi, and H.-P. Tan, Numerical analysis of two-phase electrohydrodynamic flows in the presence of surface charge convection, *Phys. Fluids* **32**, 123606 (2020).
- [66] Z. Chai and B. Shi, A novel lattice boltzmann model for the poisson equation, *Appl. Math. Modell.* **32**, 2050 (2008).
- [67] Z. Guo, C. Zheng, and B. Shi, An extrapolation method for boundary conditions in lattice boltzmann method, *Phys. Fluids* **14**, 2007 (2002).

- [68] J. Wu, P. Traoré, A. T. Pérez, and P. A. Vázquez, On two-dimensional finite amplitude electro-convection in a dielectric liquid induced by a strong unipolar injection, *J. Electrostat.* **74**, 85 (2015).
- [69] B. F. Wang and T. W. H. Sheu, Numerical investigation of electrohydrodynamic instability and bifurcation in a dielectric liquid subjected to unipolar injection, *Comput. Fluids* **136**, 1 (2016).